AIP | Physics of Fluids

Simulation and modeling of turbulence subjected to a period of axisymmetric contraction or expansion

Christopher J. Zusi and J. Blair Perot

Citation: Physics of Fluids (1994-present) **26**, 115103 (2014); doi: 10.1063/1.4901188
View online: http://dx.doi.org/10.1063/1.4901188
View Table of Contents: http://scitation.aip.org/content/aip/journal/pof2/26/11?ver=pdfcov
Published by the AIP Publishing

PHYSICS OF FLUIDS **26**, 115103 (2014)

Simulation and modeling of turbulence subjected to a period of axisymmetric contraction or expansion

Christopher J. Zusi and J. Blair Perot
Department of Mechanical and Industrial Engineering, University of Massachusetts Amherst, Amherst, Massachusetts 01003, USA

(Received 31 January 2014; accepted 27 October 2014; published online 11 November 2014)

The effect of axisymmetric contraction and expansion on isotropic turbulence and its subsequent decay are evaluated by way of direct numerical simulation. Low, moderate, and high rates of contraction and expansion are evaluated at a moderate Reynolds number using two different sets of initial conditions of isotropic turbulence. The initial turbulence is generated via mechanical mixing so that the large scales of the turbulence develop naturally. Length scales, decay rates, anisotropy, and two-point correlations are investigated both during and after the straining process, with the goal of quantifying how anisotropic turbulence behaves during return-to-isotropy. © *2014 AIP Publishing LLC*. [http://dx.doi.org/10.1063/1.4901188]

I. INTRODUCTION

Homogeneous axisymmetric decaying turbulence is perhaps the simplest turbulent flow in which the return-to-isotropy process can be observed and analyzed. It has a direct application to the ocean and atmosphere where the density stratification affects the vertical but not the horizontal directions. It also has applications in rotating turbulence, where correlations tend to be stronger along the rotation axis and to magneto-hydrodynamic turbulence (in stars and interstellar matter). Axisymmetric turbulence can be generated many different ways. However, this work is focused only on axisymmetric turbulence that is generated by the axisymmetric straining, both expansion (AXE) and contraction (AXC), of the mean flow, and the subsequent decay of that turbulence. The axisymmetric straining process allows this work to precisely control how the anisotropy is generated. It produces a turbulent initial condition for anisotropic decay that is easily reproduced by other experiments and simulations. This work adds to a set of canonical-strain test cases that are being produced to help explore the anisotropic energy cascade and turbulent decay process. The accompanying results for decaying isotropic turbulence (Perot[1]) and plane strain (Zusi and Perot[2]) are previously published.

Perhaps the earliest work on turbulence subjected to axisymmetric mean strain was by Taylor.[3] Eventually these and other experiments by Townsend[4] and Tucker and Reynolds[5] formed the basis for the analytical theory of Batchelor and Proudman[6] that is now referred to as Rapid Distortion Theory (RDT). RDT is a linear theory that is exact in the limit of very strong strain rates. It is used in this work to validate the numerical simulations. However, this paper is focused on the nonlinear return-to-isotropy aspects of the problem, when the strain rate is small, or after the straining is stopped entirely. The theoretical basis for understanding axisymmetric turbulence dates from Chandrasekhar[7] and continues to evolve (Matthaeus and Smith,[8] Cambon and Scott,[9] and Ould-Rouiss[10]). These works focus on mathematical representations for the two-point correlation tensor in the case where one direction is different.

The first experiments investigating the return to isotropy of axisymmetric strained turbulence were by Uberoi.[11] Uberoi[12] investigated axisymmetric contraction experimentally with a 4:1 contraction duct. He found that after the strain is completed the larger components of mean-square turbulent velocities v^2 and w^2 lose energy due to viscosity and due to the transfer of energy to the smaller component u^2. However, u^2 can receiving more energy by transfer than it losses by decay and can be seen to increase initially.

Later, Comte-Bellot and Corrsin[13] conducted experiments on axisymmetric contraction studied over a range of Reynolds numbers. And in an important paper, the experiments of Le Penven, Gence, and Comte-Bellot[14] indicated that different values of the Rotta constant are required for the Rotta[15] linear return-to-isotropy model. Lumley and Newman[16] and Choi and Lumley[17] investigated axisymmetric contraction and expansion using grid generated turbulence and determined that return-to-isotropy does not follow Rotta's linear model. Sjogren and Johansson[18] conducted wind tunnel experimental investigations of axisymmetric contraction, trying to determine the slow pressure-strain dependence on Reynolds number and on the degree of anisotropy. Ertunc and Durst[19] provide the most modern experimental data set and excellent review of the problem. Banerjee, Ertunc, Koksoy, and Durst[20] use this data set to evaluate a number of rapid pressure strain rate models and return-to-isotropy models. This last paper confirms that one-point statistics are insufficient to model either the rapid pressure strain process or the slow pressure strain process which is also referred to as return-to-isotropy.

One of the earliest numerical simulation studies of decaying axisymmetric turbulence was by Schumann and Patterson[21] where calculations with 32^3 mesh points were performed. Over time, higher resolutions have been used. For example, Lee and Reynolds[22] and Biferale *et al.*[23] used a large ensemble of 128^3 simulations to explore axisymmetric turbulent decay. An highly informative LES was of this flow was later performed by Chasnov.[24]

The earliest attempt to model axisymmetric turbulence was perhaps the DIA model of Herring.[25] This was then extended to EDQNM models by Nagauchi and Oshima[26] and the technique continues to be used to understand the problem.[27] Recent modeling approaches that involve representations of turbulence structure, Kassinos[28] and Martell and Perot[29] have also shown promise for modeling the nonlinear-return to isotropy of anisotropic turbulence. This work provides an additional data set for tuning of these models.

This work differs from prior simulations in a number of ways. First, significant care is taken in this work on the generation and subsequent resolution of the large scale eddies. It is now well understood from the theory of Saffman[30] that the large scale eddies (low-wavenumber behavior of the spectrum) has a strong influence on the observed decay rates. The practical importance of resolution for the large scales of DNS was first pointed out by de Bruyn Kops and Riley[31] and has been reaffirmed by del Alamo and Jimenez[32] for channel flow, and Perot[1] for decaying turbulence. It is likely that large scales have an equally important impact on the closely related return-to-isotropy process of interest in this work. For this reason, the initial turbulence spectrum, and particularly the low wavenumbers eddies, are generated naturally via a physical mixing process, and are not specified by an *ad hoc* initial condition for the spectra or for the low wavenumber forcing of the spectra. In addition, a mesh resolution of 512^3 is used in this study to ensure that the large scales are well resolved at all times during the simulation. Finally, this work will be interested in the two-point structure of the turbulence, not just the one-point velocity fluctuation energies.

Recent modeling approaches that involve representations of turbulence structure, Kassinos[28] and Martell and Perot[29] have shown promise for modeling the nonlinear-return to isotropy of anisotropic turbulence. This work provides an additional data set for tuning these models.

II. SIMULATION METHODOLOGY

A. Overview

In axisymmetric contraction two of the components of the mean flow contract toward the center of the domain while the third component is allowed to expand to maintain the condition of incompressibility. Therefore, in this work, the axisymmetric mean flow contraction is defined as $\bar{\mathbf{u}} = (Sx, -\frac{1}{2}Sy, -\frac{1}{2}Sz)$. Conversely, axisymmetric expansion is defined as $\bar{\mathbf{u}} = (-Sx, \frac{1}{2}Sy, \frac{1}{2}Sz)$ where in both cases S is a constant.

This type of flow is typically produced in a wind tunnel with an expanding or contracting duct, but the numerical simulations in this work use a deforming periodic box. Large expansion cases cannot be performed in a wind tunnel due to separation but they can be accomplished with a deforming box domain. An example of the domain deformation during the straining process is

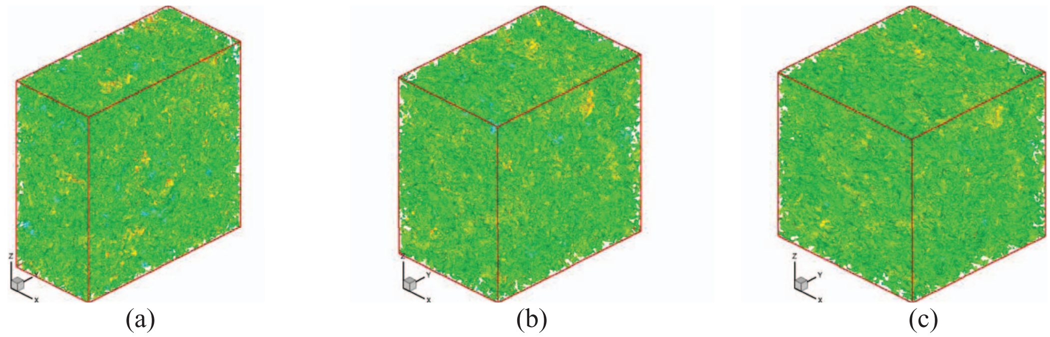

FIG. 1. Evolution of domain and turbulence during axisymmetric contraction (y and z contract while x expands). The figures show an iso-surface of the kinetic energy. (a) Pre-strain domain. (b) Half way through strain. (c) Final cubic domain. Note that the domains are not to scale.

shown in Figure 1 for axisymmetric contraction. The final domain is cubic (Figure 1(c)) since it is the return-to-isotropy from this strained state that is of primary interest in this work.

The overall simulations progress in 4 stages as shown in Figure 2. The straining with mesh motion (shown in Figure 1) occurs within stage 3 of the simulations following the generation of isotropic turbulence in stages 1 and 2. Decay of the anisotropic turbulence occurs in stage 4. In this last stage the mesh is stationary and uniform. The first two stages of the simulations involve the generation of initially isotropic turbulence and are the most computationally intensive. In the first stage the simulation is started with zero pressure and zero velocity and the domain is "shaken" with a uniform external acceleration that varies randomly in time. During this stage the domain contains small solid cubes that cause turbulent mixing to occur. Stage 1 shown in Figure 2 has fluid contours hidden for visual purposes in order to reveal the cubes. These cubes are used in a similar manner to the wire mesh used in wind tunnel experiments. In this way, all large turbulence scales are created by the Navier-Stokes equations. The first stage is detailed in Sec. II C and in Perot.[1] At the end of stage 1 the shaking stops. During stage 2 the small mixing cubes are removed and the resulting isotropic turbulence is allowed to decay until it reaches the theoretically expected decay rate. The decay rate is a far more sensitive measure of the isotropic decay than most traditional measures (such as the velocity derivative skewness).

B. Numerical method

For these simulations, the incompressible Navier-Stokes equations with constant viscosity are solved with the classic 2nd-order Cartesian staggered mesh spatial discretization of Harlow and

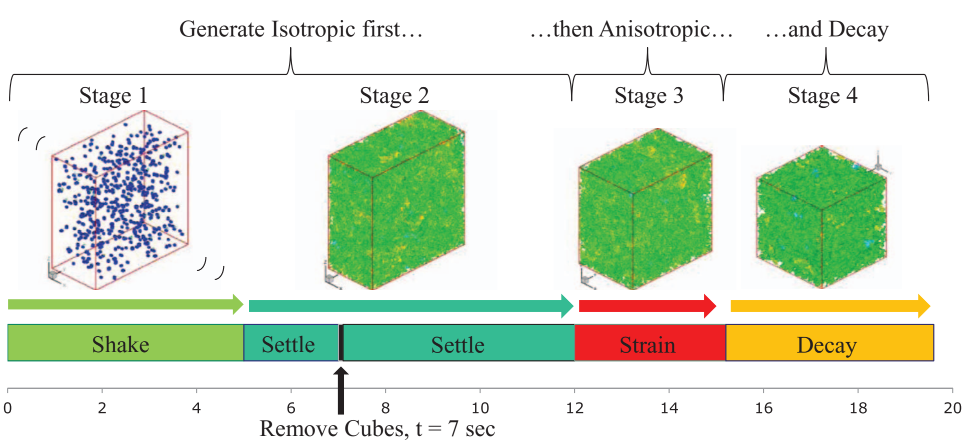

FIG. 2. Generating isotropic and anisotropic turbulence. Stage 1: "Shake" domain (t = 0–5). Stage 2: Allow for settling (t = 5–7), remove stirring cubes (t = 7), and allow for additional settling (t = 7–12). Stage 3: Strain (t = 12+). Stage 4: Allow for decay and return to isotropy.

Welch.[33] A 3-step and 2nd-order low-storage Runge-Kutta method is used for time advancement. The pressure and incompressibility constraint are enforced by using the classic fractional step method of Perot,[34] or the exact projection method of Chang *et al.*[35] The inviscid, no penetration, boundary condition is directly enforced on walls with this discretization because the normal velocity flux on a wall is a primary unknown of the method.

This numerical discretization has been widely used for turbulence simulations when complex wall boundary conditions are present (see Perot and Moin,[36] Le and Moin,[37] Martell *et al.*[38] and the references therein). This method is favored because it not only conserves mass and momentum like finite volume and spectral methods but because it also conserves secondary variables such as vorticity and kinetic energy. The kinetic energy cascade is central to the correct physical prediction by any DNS simulation, so it is attractive to know that this discrete system respects the energy and vorticity physics of the Navier-Stokes equation system. The method is validated in Sec. II D. Numerical methods with attractive secondary conservation properties are discussed extensively in Perot,[39] and a general methodology for generating such discretizations can be found in Perot and Subramanian.[40]

Fourier spectral methods are common in DNS simulations of turbulence and were used for all the previously cited simulations of axisymmetric turbulence. However, in the situation where turbulence arises physically from mechanical stirring and is not imposed as an *ad hoc* initial condition or due to *ad hoc* large scale forcing terms, Fourier spectral methods are not appropriate. The required no-slip wall boundary conditions cannot be imposed with an inherently periodic Fourier spectral method. The reader should be cautioned that Fourier methods are not significantly more accurate than a physics capturing (mimetic) 2nd order methods for DNS simulations. The described method resolves small scale fluctuations (dissipation spectra) just as well as FFT based methods with the same resolution (Sec. II D). Neither numerical method is operating at a super-fine mesh resolution where mathematical order of accuracy arguments would apply.

C. Turbulence generation

The generation of the turbulence is a relatively important component of this work because the large length scales are allowed to develop naturally rather than being imposed by any prescribed initial condition or large scale forcing. For the simulations shown in this work 768 small no-slip cubes are randomly distributed throughout the domain. These small mixing cubes fill less than 2% of the total fluid volume.

The cubes remain fixed in place and the turbulence is generated by imposing an external, constant in space, acceleration. This is equivalent to performing the calculation in a time varying linearly accelerating reference frame (shaking). The direction of this acceleration is changed randomly every 0.3 s, but its magnitude is specified by the user. The shaking time scale is much less than the initial large eddy timescale (which is on the order of 2.0), but long enough to create a wake behind each cube that on average interacts with a neighboring cube's wake, see Figure 3. A typical value of the

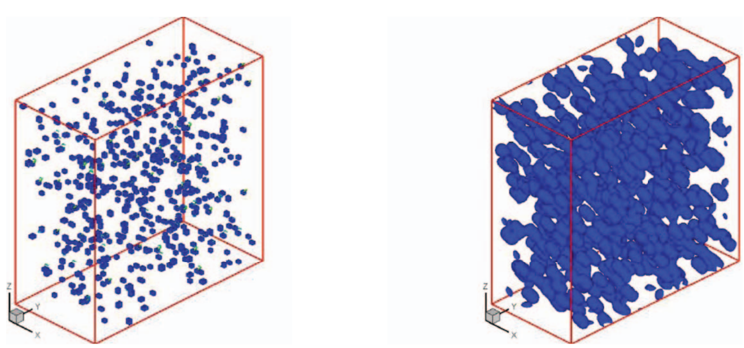

(a) (b)

FIG. 3. Stirring cubes (a) as seen just prior to the onset of shaking. (b) As shaking begins, interacting wakes are generated by the mixing cubes.

acceleration is 100 cm^2/s (or about 1/10th the acceleration of gravity). The shaking is performed for 5.1 s in most simulations (or 17 different accelerations).

The primary acceleration (shaking) is then turned off and a restoring acceleration is allowed to act for another 1.9 s. After 1.9 s the restoring acceleration (which is exponentially decaying in time) causes the mean flow to be extremely close to zero. A mean flow of zero is not necessary for the code, but it does allow the simulation to take slightly larger time steps (by minimizing the CFL stability criteria), and it does seem to lead to better statistical accuracy at very long times when the fluctuations can become smaller than the mean flow. During this 1.9 s period the turbulence changes from being accelerated to being in isotropic decay. At the end of this period (at a time of 7 s) the boxes instantaneously turn into zero velocity fluid. It tends to take about one or two large-eddy turnover times for the surrounding turbulence to fully merge with (chew up) the small regions of zero velocity fluid where the stirring boxes previously existed. Thus by a time of 12 s the flow is considered isotropic and ready for the straining process. The validity of the turbulence at time 12 s is discussed further in the section that follows. If the simulated fluid is water at standard temperature and pressure (with $\nu = 10^{-2}cm^2/s$) then the simulated domain size (after the straining) is a cube that is 48 cm on a side. The 768 randomly placed small cubes that stir the turbulence are 1.4 cm on a side. The total volume of all the stirring cubes is therefore 1.93% of the total simulation volume. The mesh size (after straining) is 0.9375 mm (which is 1/15th of the stirring cube size). During the initial shaking, the domain size and mesh are not the same size in the compressed and transverse directions. At early times in the simulation, the timestep can be as small as 1/1000th of a second. In all the simulations it is never larger than a 1/10th of a second. All the simulations run out to a time of roughly 110 s.

D. Validation

The 3D energy spectra and dissipation spectra are shown in Figures 4(a) and 4(b) at a time of 12 s (solid lines) for IC2. These spectra (solid lines) are compared with experiments. Symbols are data from the second measurement station of Compte-Bellot and Corrsin[41] (tU/M = 98). The Compte-Bellot and Corrsin experiments have a Taylor microscale Reynolds number of 65.3 at this measurement station. The current simulations have a Taylor microscale Reynolds number of 50.8 at a time of 12 s. Both the low wavenumber and high wavenumber (dissipation spectra) are well captured.

E. Moving mesh for straining

When the fluid is being strained, the simulations are performed on a moving mesh that moves with the mean flow. The incompressible Navier-Stokes equations in an arbitrary moving reference

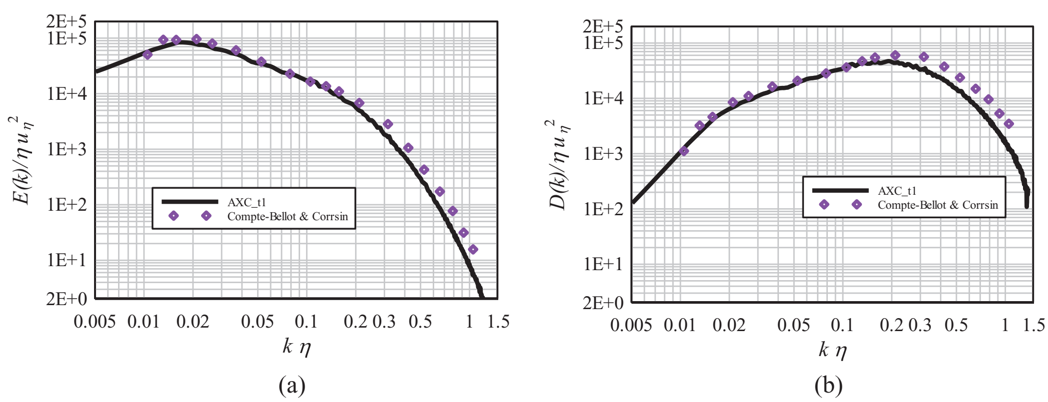

FIG. 4. (a) 3D Energy spectra. (b) Dissipation Spectra. Solid lines (black) are the current simulations at time 12 s. Symbols are from Compte-Bellot and Corrsin[41] at tU/M = 98 (second station).

frame, **v**, and with kinematic pressure, p, are

$$\frac{\partial \mathbf{u}}{\partial t} + (\mathbf{u} - \mathbf{v}) \cdot \nabla \mathbf{u} = -\nabla p + \nu \nabla^2 \mathbf{u}, \tag{1a}$$

$$\nabla \cdot \mathbf{u} = 0. \tag{1b}$$

The equation for the mean velocity, which for the case of plane strain is constant in time and varies linearly in space, then becomes

$$(\bar{\mathbf{u}} - \mathbf{v}) \cdot \nabla \bar{\mathbf{u}} + \nabla \cdot (\overline{\mathbf{u}'\mathbf{u}'}) = -\nabla p, \tag{2}$$

where $\mathbf{u}' = \mathbf{u} - \bar{\mathbf{u}}$ is the fluctuating (turbulent) velocity. The second term is zero when the turbulence is homogeneous, and for these simulations the reference frame moves with the mean flow, $\mathbf{v} = \bar{\mathbf{u}}$, so the first term is also zero. This means that the mean pressure is spatially constant (and set to zero for simplicity). As a result the equation for the fluctuating velocity, $\mathbf{u}'$, in a moving frame is (in Cartesian tensor notation)

$$\frac{\partial u'_i}{\partial t} + u'_i u'_{i,j} + u'_j \bar{u}_{i,j} = -p'_{,i} + \nu u'_{i,jj}. \tag{3}$$

This has a form similar to the Navier-Stokes equations but with an extra source term (third term on the left hand side) that is due to the mean flow. For axisymmetric contraction and expansion the mean velocity gradient tensor is a diagonal tensor and the result of this extra term is to cause exponential decay (during contraction) or growth during (expansion) for the x-direction fluctuations and exponential growth (during contraction) or decay (during expansion) of the y and z-direction fluctuations. Pressure, diffusion, and advection, then modify this forcing term. In the RDT limit, the mean gradient forcing term is large and only the pressure is large enough to modify its effects. A numerical solution for the fluctuating velocity is attractive because it allows the use of periodic boundary conditions on the sides of the simulation domain. The mean flow is not periodic, but the fluctuating velocity and pressure fields can be represented as periodic fields.

In the simulations performed for this work the initial domain in which the stirring boxes reside and in which the turbulence is initially generated is not cubic. For axisymmetric contraction it is shorter in the x-direction and is given by $L_x^{initial} = L^{final} e^{-2ST}$ where L^{final} denotes the edge length of the domain (cube) at the end of straining, S is the strain rate (as defined earlier) and T is the total straining time. The initial domain for axisymmetric contraction is also longer in the y and z-directions than the final cubic domain and is given by $L_y^{initial} = L_z^{initial} = L^{final} e^{ST}$. The initial domain for the axisymmetric contraction case is depicted in Figure 2 (stages 1 and 2). As the turbulence is strained the domain grows in the x direction and shrinks in the y and z-directions Figure 2 (stage 3). Finally, at the end of the straining period the domain is cubic Figure 2 (stage 4).

Similarly the initial domain for axisymmetric expansion is constructed such that it is larger in the x-direction and shorter in the y and z-directions. Note that different strain rates can be used with the same initially distorted mesh as long as the product of strain rate and the strain time, ST, remains constant. For all the cases in this work $ST = 0.5$. If the straining starts at time = 12 s, then a strain rate of $S = 0.6251$/s, strains for a duration of 0.8 s, or until a time of 12.8 s. Similarly $S = 0.156251$/s strains for a time of 3.2 s, and $S = 0.031251$/s strains for 16 s.

After the domain becomes cubic in shape the strain is turned off. The resulting anisotropic turbulence then decays without strain and with no more motion of the underlying mesh.

III. RESULTS

A. Initial conditions

Simulations were performed for cases of both axisymmetric contraction (AXC) and expansion (AXE), each undergoing three different strain rates (low, medium, and high). In addition, in order to investigate the effects of initial conditions, two different initial conditions were used for each simulation case producing a suite of 12 simulations. The initial conditions (at the start of strain, $t_0 = 12s$) are listed in Table I. As a result of the slightly different initial values for the turbulence, the dimensionless strain rate, Sk_0/ε_0, varies slightly between the low, medium, and high strain rate cases.

TABLE I. Initial conditions for 12 test cases. All values are taken at time t = 12 s (the onset of strain).

		k_0	ε_0	Re_0	$Re_{\lambda 0}$	$T_0 = k_0/\varepsilon_0$	$L_0 = k_0^{3/2}/\varepsilon_0$	Sk_0/ε_0	L_η	$L_\eta/\Delta x$
AXC	IC1	0.706	0.131	380.417	50.360	5.388	4.527	Low = 0.168	0.053	0.561
								Med = 0.842		
								High = 3.367		
	IC2	0.719	0.141	365.016	49.330	5.099	4.324	Low = 0.159	0.052	0.550
								Med = 0.797		
								High = 3.187		
AXE	IC1	0.770	0.138	430.827	53.593	5.595	4.909	Low = 0.175	0.052	0.554
								Med = 0.874		
								High = 3.497		
	IC2	0.838	0.160	440.103	54.167	5.252	4.808	Low = 0.164	0.050	0.534
								Med = 0.821		
								High = 3.282		

Where S is the characteristic mean strain rate given by the maximum absolute strain rate in each case. The largest dimensionless strain rate cases will be shown to approximate the theory of RDT well during the straining period. The different initial conditions are generated by having different random placements for the stirring cubes, and by shaking the domain in different random directions (though at the same amplitude).

In addition to the dimensionless strain rate, Table I also contains the initial kinetic energy k_0, dissipation ε_0, initial turbulent Reynolds number $Re_0 = k_0^2/\nu\varepsilon_0$, and the initial Taylor micro-scale Reynolds number $Re_{\lambda 0} = \sqrt{(20/3)\,Re_0}$. This work is similar in initial turbulent Reynolds number and resolution to the well resolved simulations of de Bruyn Kops and Riley.[31] The turbulent Reynolds numbers present in these simulations should be sufficient to capture the fundamental physics. The turbulent Reynolds number is also nearly the same as the turbulent Reynolds numbers in the classic wind tunnel experiments of Compte-Bellot and Corrsin.[41]

The initial large-eddy turnover time $T_0 = k_0/\varepsilon_0$, is roughly 5 s. The duration of the strain is always less than or roughly equal to this time scale. The initial large-eddy length scale $L_0 = k_0^{3/2}/\varepsilon_0$ of roughly 4.8 is 1/10 of the simulation domain. The domain therefore provides considerable resolution of the large eddy scales. A domain size of at least 4 times the large eddy size was found by Perot[1] to be a necessary condition for proper decay in isotropic turbulence. Finally the Table also shows the initial Kolmogorov length scale, $L_\eta = \nu^{3/4}/\varepsilon^{1/4}$. A Kolmogorov length scale that is half the largest mesh spacing Δx or bigger is considered by most DNS practitioners to be more than sufficient for resolving small scales.

B. Time development

The behavior of the turbulent Reynolds number and the large-eddy length scale are shown as a function of time in Figure 5. This figure shows the behavior for two different initial conditions. High strain rate is shown for both AXC (Figure 5(a)) and AXE (Figure 5(b)), other strain-rate cases behave similarly. Note that the length-scales (increasing set of blue curves) grow more rapidly during the straining process (12.0–12.8 s). The Reynolds number (decreasing set of green curves) can also grow slightly during the straining because means expansion or contraction can add energy to the turbulence via the mean flow gradients. Solid lines are IC1 and dashed lines are IC2. The higher strain rate cases often show slightly more variation between the two initial conditions.

For all the cases in Figure 5 the length scales continue to increase with time. This indicates that the turbulence has not yet become completely constrained by the domain size. However, the turbulence is probably close to constrained at large times. In isotropic decaying simulations a length-scale of approximately $\frac{1}{4}$ the domain size (a length = 12 in these simulations) is found as the upper limit possible for the length scale before the domain begins to constrain the turbulence (and affect the decay results). Often the lengthscale overshoots somewhat higher than 12 before settling at that

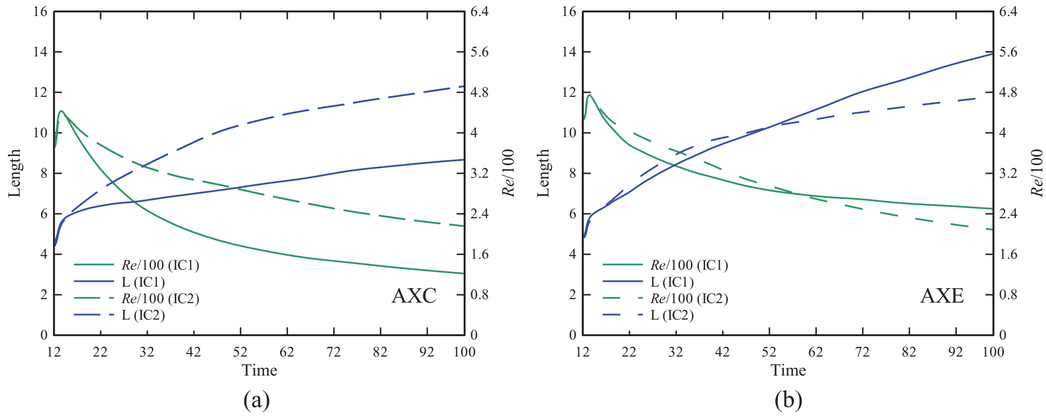

FIG. 5. Large eddy length scale (blue, increasing curves: left y-axis) and turbulent Reynolds number/100 (green, decreasing curves: right y-axis). (a) AXC and (b) AXE at high strain rate. IC1 is solid lines and IC2 is dashed lines.

value. If similar effects are happening in these simulations (with the same code and domain sizes), the results in Figure 5 are reaching a time where the periodic domain may begin to influence results. This indicates that simulation times greater than 100 may become polluted by the finite domain size.

Reynolds stresses for AXC IC1 and AXE IC2, both subjected to high strain rates, are shown in Figure 6 as they evolve in time. Again, these cases are indicative of the other strain rates and initial conditions. The Reynolds stresses decay with time overall, but for AXC there is an increase in the R_{22} and R_{33} stresses during the straining period and a more rapid decrease in R_{11}. Similarly, for AXE the opposite affect occurs. The off-diagonal components of the Reynolds stress tensor are small (statistically equal to zero) and so are not relevant to show in this figure. The blue (dotted) and green (dashed) lines would be identical to each other if the initial condition was perfectly axisymmetric. For statistical reasons, the initial conditions in this work are only ever close to axisymmetric.

In this work, the dimensionless Reynolds stress anisotropy tensor is given by the expression,

$$b_{ij} = \frac{R_{ij}}{2k} - \frac{1}{3}\delta_{ij}. \tag{4}$$

This quantity removes the effect of the strong decay that dominates Figure 6 and focuses on the deviations of the Reynolds stresses from the isotropic case. Figure 7(a) shows the anisotropy tensor corresponding to AXC for initial conditions IC1 while Figure 7(b) shows the anisotropy tensor corresponding to AXE for initial conditions IC2. Both Figures 7(a) and 7(b) show b_{ij} values as a result of low medium and high strain rates. The higher the strain rate the quicker the anisotropy

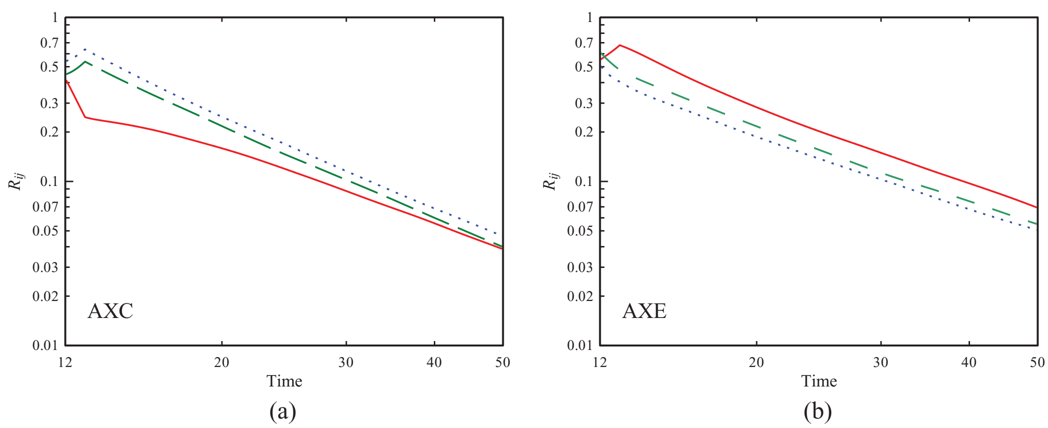

FIG. 6. Reynolds stresses for (a) AXC IC1: high strain rate. (b) AXE IC2: high strain rate. R_{11}: solid red, R_{22}: dashed green, and R_{33}: dotted blue.

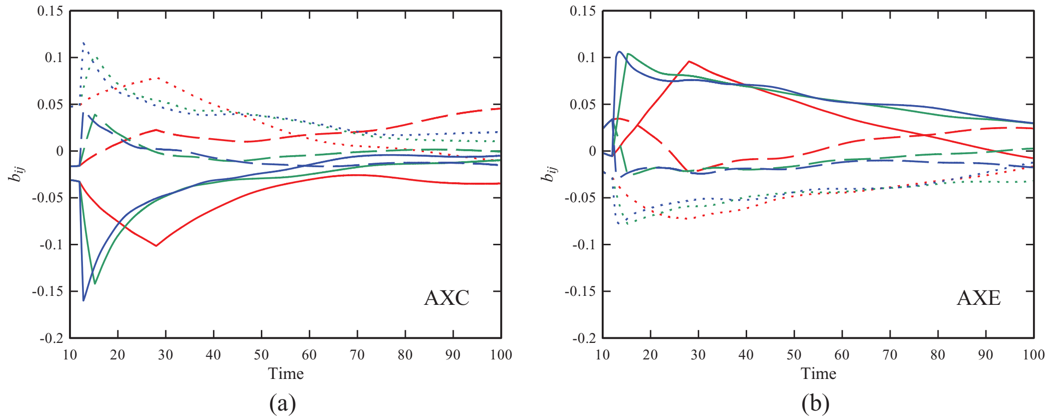

FIG. 7. Normalized anisotropy tensor (b_{11}: solid lines, b_{22}: dashed lines, b_{33}: dotted lines) showing the effects of low, medium, and high strain rates on (a) AXC IC1 and (b) AXE IC2. The straining process occurs from 12.0 until 12.8, 15.2, and 28.0, respectively. The highest strain rate cases are the ones that move away from isotropy the quickest and which peak the earliest.

grows (at early times, when the strain is on). Other than statistical noise the off-diagonal components of the tensor are zero and are not shown.

Figure 7 confirms the theoretically expected behavior of turbulence subjected to AXC and AXE. During the AXC straining process the b_{22} and b_{33} components of the tensor increase while the b_{11} component decreases. After the straining process, all the anisotropy components tend to decay back towards zero. If perfect axisymmetry of the initial conditions existed then the dotted and dashed lines would lie on top of each other. It is clear that the behavior of the two sets of curves are very similar, with the major difference being a shift due to the slightly different initial conditions. As would be expected for AXE the b_{22} and b_{33} components now decrease and become negative, while the b_{11} component increases during the expansion process. In general, regardless of AXC or AXE the tensor components aligned in the direction of contraction increase while those aligned with expansion are suppressed.

Figure 7(b) shows that at short times after the strain is removed from AXE the b_{11} component continues to increase, whereas for AXC the turbulence anisotropy abruptly decreases as soon as contraction ceases. This behavior of expansion is also seen in the case of plane strain Zusi and Perot.[2] We refer to this period after the strain is removed, but before all components begin to reduce their isotropy, as the ***recovery*** period. It is hypothesized in this work that in this ***recovery*** period the structure of the turbulence (the two-point correlation lengths) are returning to isotropy faster than the velocity fluctuations are returning. The structures quickly ***recover*** their isotropic values, while the more classic mixing of velocity fluctuations and return-to-isotropy operates on a slower time scale. Note in Figure 7(b), that recovery is more pronounced the higher the strain rate. This idea is used in the modeling Sec. IV B.

For these simulations a b_{ij} with a magnitude < 0.05 is essentially statistical noise. At long times the various tensor components can be seen to wander within ± 0.05. At very long times, the anisotropy curves do not appear to asymptote to zero. They seem to asymptote to a fixed (non-zero) value. This could be a statistical effect caused by the very largest eddies (the only ones left after very long times) not having enough statistical sample in the finite simulation domain. Experiments show similar results, Le Penven,[42] Gence[43] at long times.

Kassinos *et al.*[28] point out an interesting and counter-intuitive behavior of the anisotropy. Smaller strain rates (red lines that rise the slowest in Figure 7) can lead to the highest anisotropy levels. This unintuitive behavior is a direct result of the non-dimensionalization being used for the anisotropy measure. Larger strains tend to lead to larger kinetic energy levels, which when used in the denominator of (1a), lead to smaller dimensionless anisotropy values. Dimensional anisotropy measures ($a_{ij} = R_{ij} - \frac{2}{3}k\delta_{ij}$) show expected behavior (larger for larger strain values).

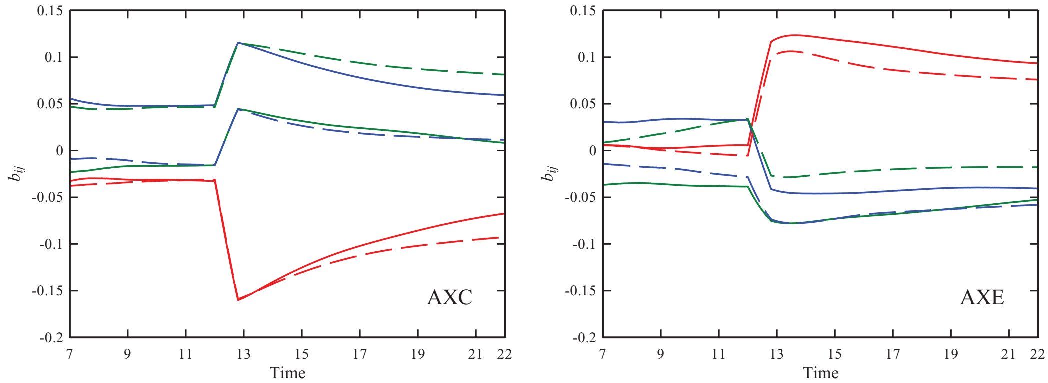

(a) (b)

FIG. 8. Effects of initial conditions on (a) AXC and (b) AXE. IC1: solid and IC2: dashed.

C. Initial conditions

Figure 8 shows the effect of having different initial conditions at the same strain rate. Figure 8(a) shows AXC and Figure 8(b) shows AXE both subjected to the highest strain rate. In both figures solid lines are IC1 and dashed lines are IC2. The highest strain case shows the most variation between initial conditions. Figure 8(b) also clearly shows the recovery region immediately following the removal of strain at time 12.8 s. This figure suggests that at high strain the recovery process described above is robust and is not a statistical artifact of IC1.

D. Scaling

Figure 9 uses a scaling of the time axis to normalize the results for b_{ij} under the action of strain. This scaling uses a dimensionless timescale based on the strain rate, $t^* = S(t - 12)$, where 12 is the time in seconds at which straining begins. Under this scaling all the curves should begin and end the straining process at the same dimensionless time. The black lines in Figure 9 are the theoretical results from the RDT theory for an infinite strain rate. The highest simulated strain rates (with dimensionless strain rate values of around 3) closely approximate the RDT theory. For AXC, the lower strain rates show a marked deviation from the RDT theory.

However, the AXE tends to agree with the RDT solution even at relatively low strain rates. The implication, here is that return to isotropy is weaker for turbulence generated by expansion.

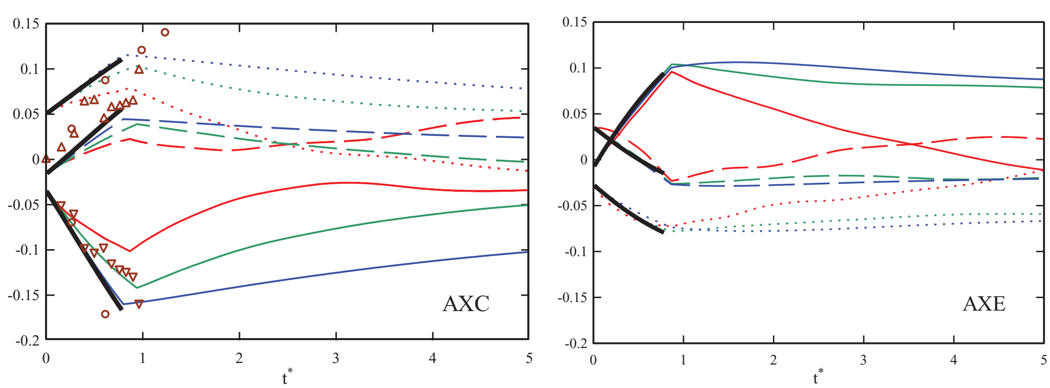

(a) (b)

FIG. 9. Component of anisotropy tensor during strain and recovery subjected to different strain rates with x-axis scaled by $S(t - 12)$. b_{11} (solid), b_{22} (dashed), and b_{33} (dotted). Triangles are experimental data of Tucker[5] ($Sk/\varepsilon = 2.1$) and circles are the DNS data of Lee and Reynolds[22] ($Sk/\varepsilon = 56$). (a) AXC IC1 and (b) AXE IC2. Note that lower strain rates diverge from the RDT predictions (thick black lines) earlier in the straining process and return faster when using the strain-normalized timescale, t^*.

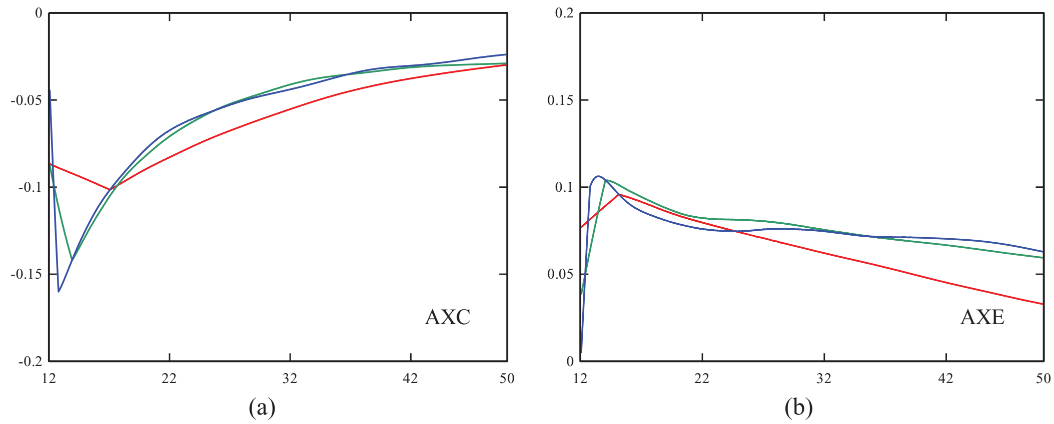

FIG. 10. b_{11} with each curve translated on the x-axis such that the point in time at which straining is stopped coincides with a point on the largest strain case allowing for a comparison of the return processes. (a) AXC IC1 and (b) AXE IC2.

Experiments (Gence *et al.*) have also noted these phenomena. We hypothesize in this work that it is not differences in the Reynolds stress anisotropy that cause this effect, but differences in the turbulence structures (specifically two-point correlations) that the two different types of straining create.

A similar scaling of the time axis, for the situation after the strain is removed is more difficult. There is no obvious timescale in this situation. The large eddy timescale $T = k/\varepsilon$ varies linearly with time. Normalizing by it means dividing time by something proportional to time. Normalizing by the initial value at a particular time (say after strain stops) is arbitrary. A similar time normalization dilemma occurs for isotropic decaying turbulence. In Figure 10 each curve is shifted in time until the peak value of the anisotropy (the value at the end of the strain) lies on the highest strain rate curve. After matching this "start time" to the highest strain curve, the subsequent evolution of the anisotropy behaves very similarly (the curves lie on top of each other) for the highest AXC strain rates. The lowest strain rate behaves slightly differently following the removal of strain. Note that time has not actually been scaled in this plot, just shifted. Also note that this observation of the flow after strain is removed, also confirms the interpretation that return-to-isotropy is a stronger process for turbulence generated by contraction than it is for turbulence generated by expansion.

E. Two-point correlations

The longitudinal correlations, f, are shown in Figure 11 for the highest strain case and first initial condition (IC1). The other initial conditions and strains look essentially the same. Both the longitudinal correlation in the direction of maximum stretching, (f_{11}, red curves, lower set for AXC and upper set for AXE) and the average longitudinal correlation in the direction of minimal stretching (f_{22}, black curves) are shown. Each figure also shows three different times. The time just before straining ($t = 12$), where the turbulence should be isotropic is given by dotted curves. The time just after strain ends ($t = 12.8$ for this case) is given by dashed curves. Finally, the correlations at two large-eddy turnover times (K/ε) after the strain is done ($t = 22$) are shown with solid curves. The correlation separation distance, r, has been normalized by the large-eddy lengthscale ($K^{3/2}/\varepsilon$) evaluated at that time.

The AXE (Figure 11(b)) starts very isotropic. The two initial correlations (dotted lines) lie nearly on top of each other. Strain causes very little change in the f_{11} correlation (upper set of curves, red) showing that this correlation scales very well with the large-eddy length scale. In contrast, strain causes the f22 correlation to drop, indicating a reduction in the eddy lengthscale in this direction. After the strain has been removed, the effect is reversed. The f_{11} correlation now changes significantly and scales with a larger lengthscale than $K^{3/2}/\varepsilon$, and the f22 correlation does not change much compared to the correlation after strain (at $t = 12.8$, dashed line). The net result

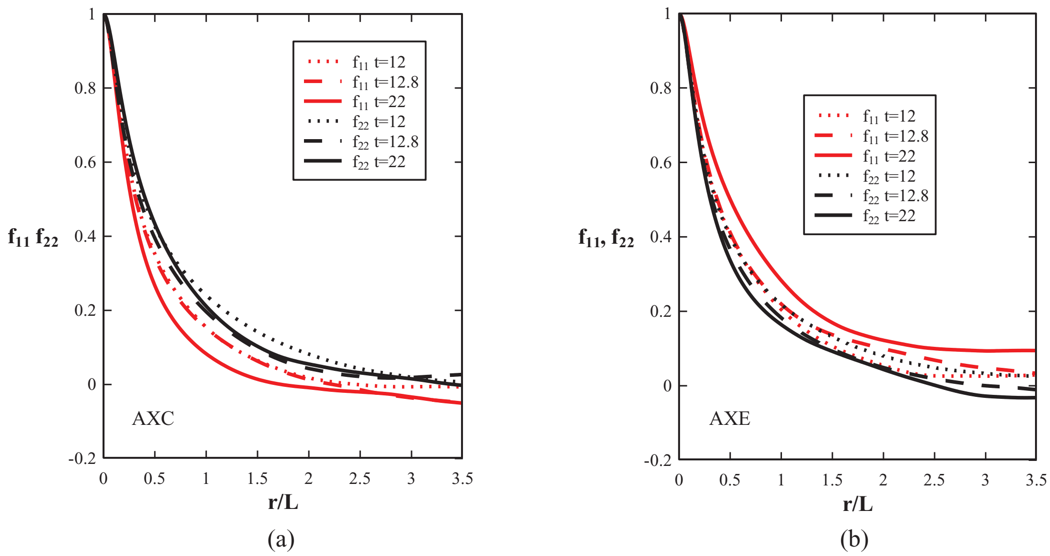

FIG. 11. Longitudinal correlations in the max stretch (f_{11}) and minimum stretch (f_{22}) directions at times before (t = 12) and after strain (t = 12.8) and a final time well after strain is removed (t = 22). (a) AXC with f_{11} being the lower set of three curves (red) and f_{22} being the upper set of three curves (black). (b) AXE with the two groups of correlations reversed in their locations (f_{11} on top).

of axisymmetric expansion is an increase in the lengthscale in the direction of maximum magnitude strain and a decrease in the lengthscale in the other two directions.

The situation for AXC is consistent with this picture, but is slightly complicated by the fact that the turbulence is not initially completely isotropic. The two dotted curves for Figure 11(a) (the before strain curves) do not lie on top of each other. The effect of anisotropy is addressed in Figure 12 and the accompanying text. As with expansion, for contraction the max strain direction f_{11} (lower set of curves, red) does not change under the influence of strain (using the large-eddy scaling for the separation distance, r) but does change (with lengthscales getting smaller now) during the return process. As with expansion, the minimum strain direction f_{22} does change during strain (getting a larger lengthscale) but not during the return to isotropy process.

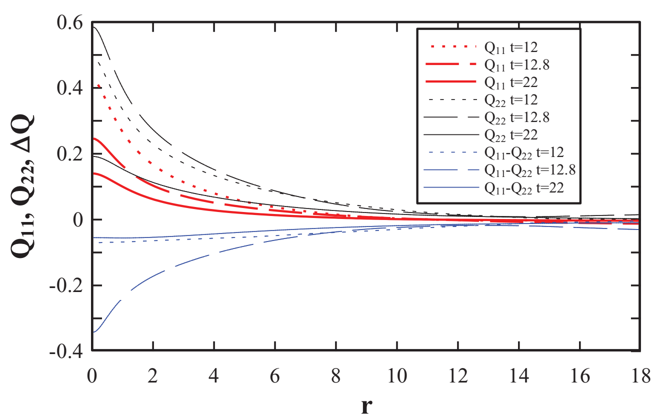

FIG. 12. Unnormalized two-point correlations for axisymmetric contraction. Thicker (red) curves are the correlations in the maximal strain direction. Thinner (black) positive lines are the minimal strain direction two-point correlations. At a given time these are always larger than the previous set of curves. The bottom (blue) set of negative curves are the difference between the two. Dotted lines are before strain. Dashed lines are right after strain completes and solid lines are at two large-eddy turnover times after the strain is completed.

The two-point correlations for AXC are shown in Figure 12 unnormalized. In this figure $Q_{11} = \overline{u_1(\mathbf{x})u_1(\mathbf{x}+r_1)}$ and $Q_{22} = \overline{u_2(\mathbf{x})u_2(\mathbf{x}+r_2)}$ which are the unnormalized f_{11} and f_{22} curves. In addition to the same curves shown in Figure 11, a third group of curves has been added which is the difference between the two correlations (at each time). This third group is always negative in this case. This figure shows that before the strain is imposed (dotted lines), the difference between the two-point correlations is almost constant and decreases very slowly with separation distance. The large-eddy lengthscale varies from 4.5 to 6.4 over times shown here. This indicates that the anisotropy in this initial condition is due to the presence of a few very large eddies (that presumably in this particular case do not cancel out well because of their small number within the simulation domain). After strain (dashed line), the anisotropy between the two is much larger and dominated by the strain. However, it can be seen that after a few large-eddy turnover times after the strain is removed the correlations do not return completely to isotropy. Instead they return to the initial large-scale anisotropic state. We hypothesize that the largest eddies in the system cannot return to isotropy easily because there are not even larger eddies to mix them up and force this isotropization. Note that this figure implies that the better way to correct these correlations in order to remove the large scale statistical anomaly effects is not to scale them by their peak values (at r = 0), but to subtract the large scales (which are nearly constant and therefore given by the Reynolds stress anisotropy levels).

F. Invariant map

The anisotropy invariant map[44] is a common way to look at the return-to-isotropy problem. The anisotropy tensor has zero trace, so the state of the turbulence anisotropy can be described by the other two invariants, $II = -(1/2)b_{ij}b_{ji}$ and $III = (1/3)b_{ij}b_{jk}b_{ki}$. Figure 13 shows the variation of the turbulence anisotropy invariants (for the highest strain rate cases) as it progresses through the straining process and then through the decay process for both (a) AXC and (b) AXE. Both sets of initial conditions are shown. In all four cases, the turbulence starts close to the origin (isotropy). The solid red lines, no symbols, show the evolution as the turbulence is strained and moves away from isotropy. When the strain is removed (colored symbols) the state generally moves back toward $-II = 0$, $III = 0$ (return-to-isotropy). An equal amount time exists between the symbols during each of the decay processes shown. The return-to-isotropy process slows as the turbulence becomes more isotropic. At very long times the trajectories tend to wander without a clear direction towards the origin. It is believed that this is the result of the fact that at long times the simulations are corrupted by the influence of the finite domain size. The two initial conditions produce somewhat different trajectories due to differences in their initial states, but the overall affect of the strain and subsequent decay are still clear in each case.

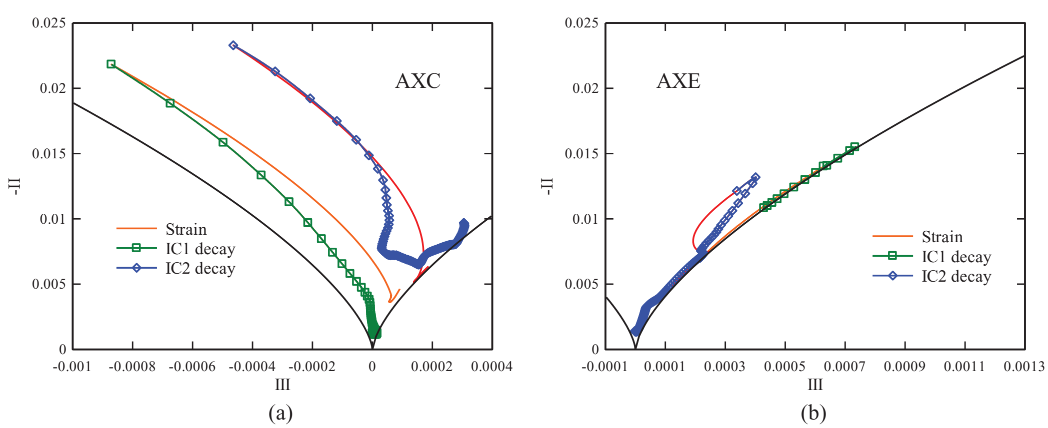

FIG. 13. Invariant plots of Reynolds-stress anisotropy subjected to high strain rates: (a) AXC and (b) AXE. The lowest black curves bound the realm of realizability. Solid red lines show the trajectory during the straining process and lines with symbols show the anisotropic decay trajectories.

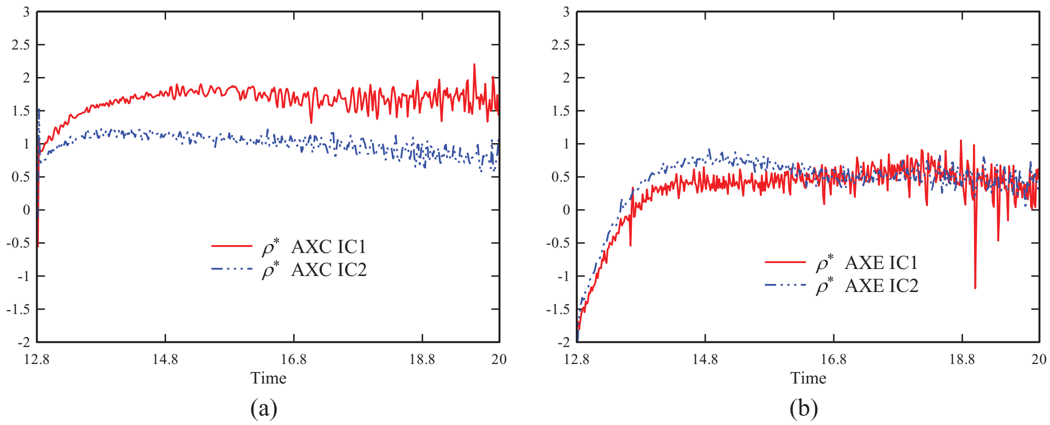

FIG. 14. Comparing relative return rates of AXC and AXE. ρ^*, Eq. (1a), is a ratio of the time scale of decaying turbulent kinetic energy to that of return-to-isotropy.

The rate of return to isotropy can be quantified by the expression,

$$\rho^* = \frac{k/(dk/dt)}{II/(dII/dt)}, \tag{5}$$

which compares the rate of decay of the kinetic energy to the rate of decay of the second invariant. Choi and Lumely[45] found experimentally values of ρ^* for AXC cases are approximately 2.5 times larger than for AXE cases. Figure 14 shows a similar effect for these data. With AXC (Figure 14(a)) returning 2.5 times faster for short times and up to 4 times faster at longer times than AXE (Figure 14(b)).

Figure 15 shows the effect of the variation in strain rate on both AXC and AXE. Figures 15(a) and 15(c) show AXC IC1 and AXC IC2, respectively, while Figures 15(b) and 15(d) show AXE IC1 and AXE IC2, respectively. Each of the four plots shows the effects of the three different strain rates. For the AXC cases the tendency during the return process (lines with symbols) is for the turbulence to seek a trajectory that lies closer to the $-III$ boundary of realizability (solid, black curve beneath and to the left of the strain/decay curves) than their preceding strain trajectories. This boundary is the limit of perfectly axisymmetric turbulence (with two large and one small Reynolds stress). It also appears that during the straining process the lower the strain rate the more the tendency to move toward the $-III$ boundary. This motion towards axisymmetry is thought to be a result of the nonlinear return-to-isotropy process. Nothing in linear RDT theory would suggest this behavior.

The AXE cases exhibit significant differences from IC1 to IC2. For IC1 (Figure 15(a)) the different strain rates produce very similar results moving up and back immediately adjacent to the $+III$ boundary of realizability both during the strain and return processes. The $+III$ boundary represents perfectly axisymmetric turbulence with one large and two small Reynolds stresses. IC2 (Figure 15(b)) shows different behavior from one strain rate to the next. At the onset of strain the strain-rate trajectories immediately diverge only to align again prior to the termination of strain. It is thought that the strain is acting on some transient particular to that initial condition at early times in the straining process. The lowest strain rate shows significant divergence from higher strain rates both during the straining process as well as during return-to-isotropy. Upon removal of strain the lowest strain rate trajectory reverses direction and for a time decays back along its strain trajectory. The two highest strain rates return closer to the $+III$ boundary than their respective strain trajectories. Upon removal of the highest strain rate the turbulence continues to become slightly more anisotropic (for a short time) before evolving toward the $+III$ boundary and back towards isotropy. This is the "recovery" stage noted earlier, which is also found to occur in turbulence subjected to plane strain Zusi and Perot.[2]

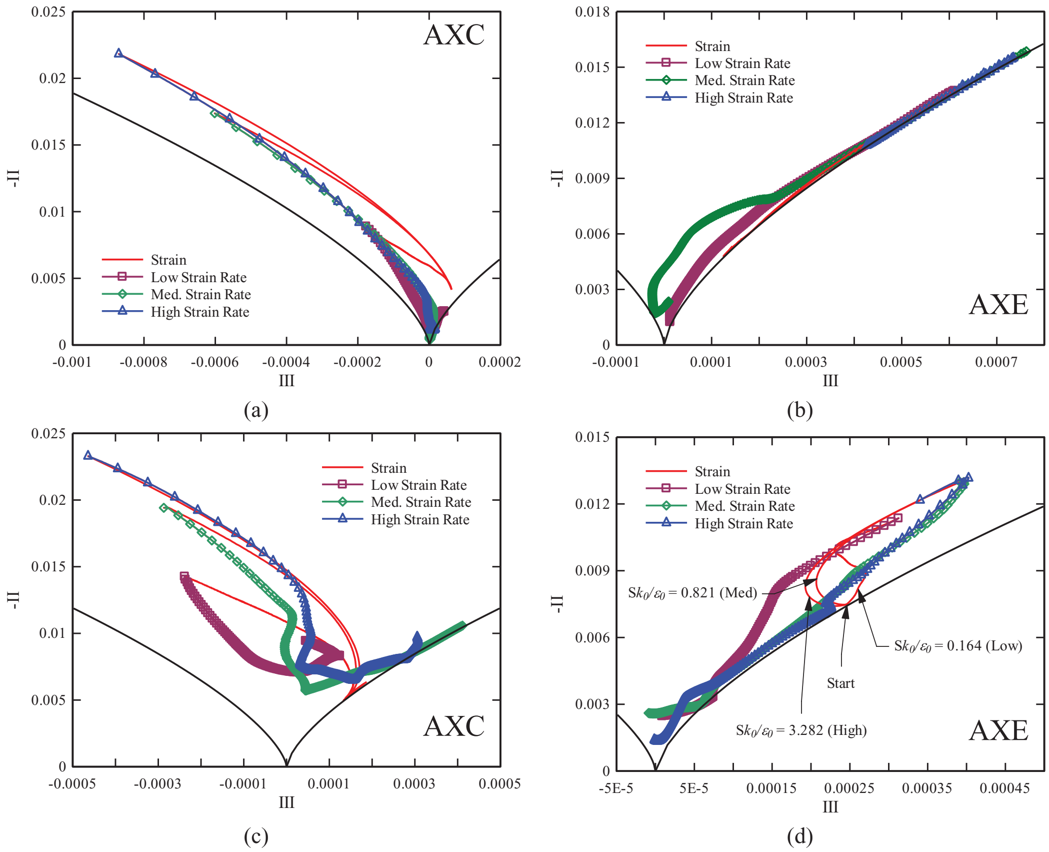

FIG. 15. Invariant maps showing the straining process (red lines no symbols) and the return-to-isotropy process (symbols). AXC: (a) IC1 and (c) IC2. AXE: (b) IC1 and (d) IC2.

G. Decay rate

Figure 16 shows the decay rate, n, as a function of time with two sets of initial conditions subjected to the high and low strain rates of both AXC and AXE. The decay rate is a sensitive measure of the energy cascade. It represents the power at which the kinetic energy decays, $K = K_0(t - t_0)^{-n}$ and is calculated via the expression, $n = [\frac{d(K/\varepsilon)}{dt}]^{-1}$. The numerical calculation of this quantity requires small time increments for an accurate representation of the derivative.[1] Before the strain is applied at time 12 the turbulence usually approaches the theoretically expected Saffman[46] high Reynolds number value of 6/5 (shown with a dashed black line on the figures). The low Reynolds number Saffman value of 3/2 is also shown on the figures.

The low strain rate cases of both AXC and AXE, Figures 16(a) and 16(c), respectively, do not significantly change the decay rate. However, the high strain cases Figures 16(c) and 16(d) show a significant reduction in the decay rate just after the strain is removed. This is due to the disruption to the energy cascade that strain (or any external forcing) produces. Disruption of the energy cascade leads to less energy dissipation, less loss of turbulent kinetic energy with time, and a smaller n. After the strain is removed the decay rate can be seen to increase significantly with time, in the cases of high strain rates, in order to recover to the theoretical values (in the theoretical limits between 1.2 and 1.5). The decay exponents of the low strain rate cases also increase but much less adjustment to the decay rate is needed for them to enter the region of 1.2–1.5 limits. In most cases of both AXC and AXE, after a long enough time, the decay rate appears to approach the low Reynolds number Saffman theoretical value of 1.5. In at least one case (AXC IC2) the decay exponent eventually moves towards the domain constrained value of 2[47] at very long times (after about 100 s). Perot[1] looks at the effects of Reynolds number on decaying turbulence in more

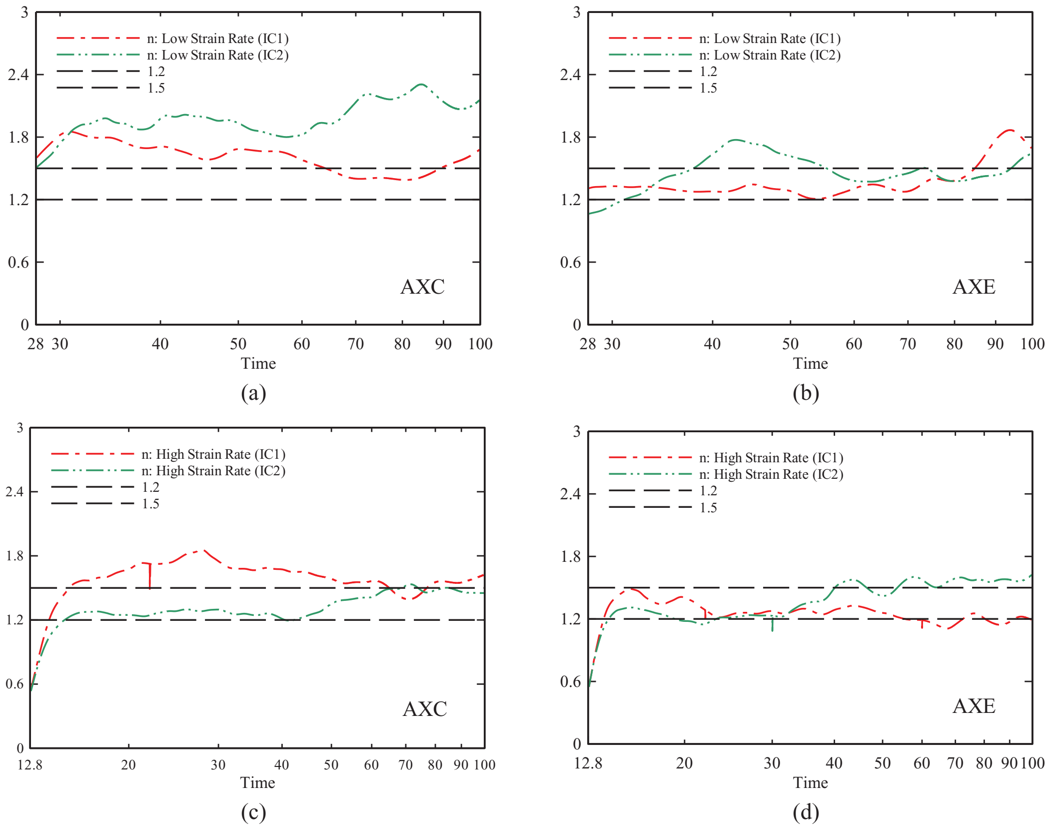

FIG. 16. Decay exponent, n, for AXC (a) and (c) and AXE (b) and (d). Resulting from the exposure of initial conditions IC1 and IC2 to low strain rates (a) and (b) and high strain rates (c) and (d).

detail and shows that the decay rate transition from 1.2 to 1.5 is not solely related to the Reynolds number.

IV. MODELING

A. Anisotropy based models

The linear model of Rotta,[15] or the more general nonlinear models (such as Sankar and Speziale[48]), attempt to represent the return-to-isotropy using only the anisotropy tensor itself. A typical model for return-to-isotropy takes the form,

$$\frac{db_{ij}}{dt} = (1 - C_1)\frac{b_{ij}}{T} + C_1^n \frac{\left(b_{ij}^2 - \frac{1}{3}b_{kk}^2\delta_{ij}\right)}{T}. \tag{6}$$

It can be seen that in order for this model to allow for return-to-isotropy the value of C_1 must be greater than 1 (see Durbin and Reif[49] for more details). The values for the constants C_1 and C_1^n can be reverse calculated from the DNS data and are shown in Figure 17 for both initial conditions of AXC and AXE.

Since these are constants for a return-to-isotropy model we are only interested in their values after the strain is removed, which in all cases in Figure 17 is after 12.8 s. Even for the same strain rate there is significant variation of these constants as a function of time and between different initial conditions. These results indicate that such a model, with any fixed set of constants would have difficulty producing accurate result for this variety of turbulence conditions.

References 16 and 50 contain examples of models where such constants are functions of the anisotropy invariants (II and III) or other dimensionless variables such as the Re. However, as

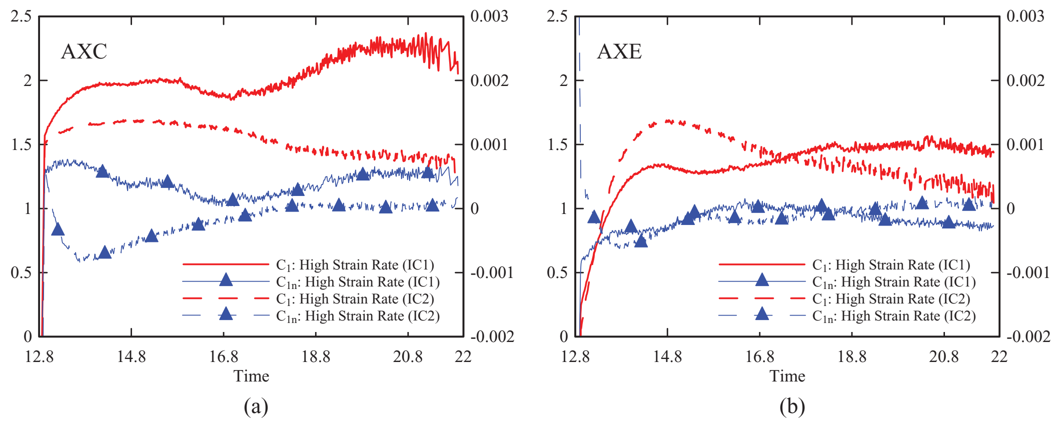

FIG. 17. Constants for the nonlinear model Eq. (6). c_1: left y-axis and c_1^n: right y-axis. High strain rate: (a) AXC IC1 (solid) and IC2 (dashed) and (b) AXE IC1 (solid) and IC2 (dashed).

discussed in Pope,[51] no matter how complex the functional dependence of the model constants, a return-to-isotropy model that only depends on information contained in the anisotropy tensor produces unique trajectories on the invariant map that never cross one another back to the origin (isotropy). For these types of models, any particular starting point on the invariant map cannot produce different evolutionary paths (trajectories) back to isotropy. Figure 15 shows return trajectories that have crossing paths during their return-to-isotropy and thus these DNS data suggest that additional information must be used in return-to-isotropy models. Section IV B discusses the performance of a model which accounts for additional information in the form of eddy structure by way of two-point correlations.

B. Oriented-eddy collision (OEC) model

The OEC model is discussed in Martell and Perot.[29] This model looks like a collection of Reynolds stress transport equations coupled with a set of transport equations for the inverse two-point correlation lengths. The information contained in the OEC model can be used to approximate the two-point velocity correlations (not just their peak values, which are the Reynolds stresses). In the OEC model the two-point correlation is approximated by

$$Q_{ij}(\boldsymbol{x}, r) = \sum \hat{R}_{ij}\left(\boldsymbol{x}, t\right) f\left(\left|\boldsymbol{q}\left(\boldsymbol{x}, t\right)\right| \cdot \boldsymbol{r}\right), \tag{7}$$

where $\hat{R}_{ij}\left(\boldsymbol{x}, t\right)$ and $\boldsymbol{q}(\boldsymbol{x}, t)$ are determined by the model and the function f is usually chosen to be a decaying exponential. The OEC model uses a classic linear return-to-isotropy model for the velocity fluctuation and also the simplest possible linear return-to-isotropy model for the inverse correlations lengths, $\boldsymbol{q}$. However, the time scale for the $\boldsymbol{q}-recovery$ is faster than that of the velocity-return.

The ability of the OEC model to predict both AXC and AXE strain and return-to-isotropy is shown in Figure 18. This figure shows the Reynolds stresses for both cases subjected to high strain rates. The OEC model is exact in the large strain RDT limit, so the ability to capture the effect of straining (early portion of the figure, where the stresses are moving apart) which is normally quite difficult for turbulence models is not a problem for this model (exact RDT is also possible with the IPRM model of Kassinos and Reynolds.[52,53] The subsequent anisotropic decay (return-to-isotropy, where the stresses are moving together) is not exact for the OEC model but the agreement over both test cases (with the same model constants) is reasonable. The OEC model uses the same information necessary to exactly capture RDT to also model the recovery process. The idea of using RDT as a modeling guide was first proposed by Kassinos *et al.*,[28] and has some similarity with the DIA model of Herring[25] and EDQNM models.[26]

A more sensitive test of the OEC model is to plot the results on the anisotropy invariant map as shown in Figure 19. Here the OEC model can be seen to produce the correct qualitative features for

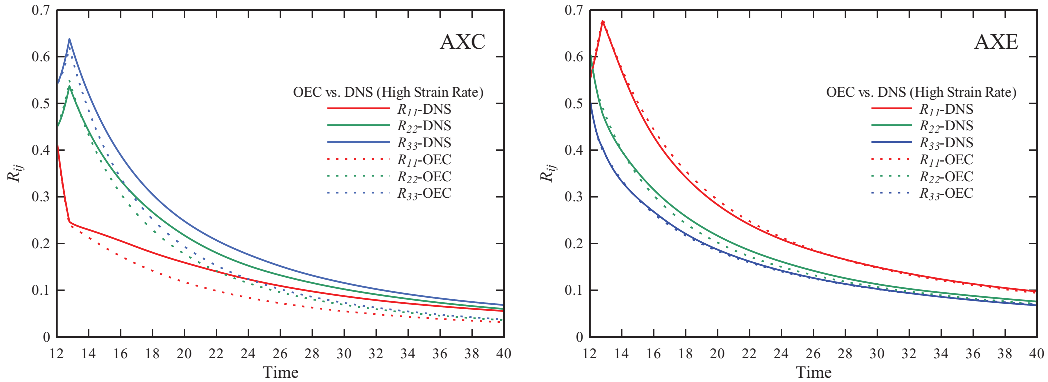

(a) (b)

FIG. 18. Reynolds stresses for AXC IC1 (a) and AXE IC2 (b). DNS data (solid lines) and the OEC model (Ref. 29) predictions (dashed lines).

cases of both AXC and AXE. The straining process is exponentially sensitive to initial conditions, and therefore the OEC results do not progress along exactly the same trajectories as the DNS simulations. These results were produced by initializing the model with the R_{ij} initial conditions only. It is thought that incorporating not only the correct R_{ij} initial conditions but also the correct two point correlations length scale initial conditions will aid in the model's performance. The capability of incorporating information from the two-point correlation initial conditions is currently being incorporated into the model.

V. DISCUSSION

The simulations presented in this work add to a growing set of canonical-strain test cases of the affect of strain on isotropic turbulence and its post-strain return-to-isotropy. These simulations have a 512^3 mesh resolution in order to resolve and capture the large scales accurately. The large scales are known from theory to govern the behavior of isotropic decay. They also appear to strongly influence the behavior of anisotropic turbulence.

The initial conditions for the presented simulations were generated by mechanically stirring the fluid. This is done in the numerical simulation by moderate size no-slip cubes. This is done so that all large scale turbulence is formed by the turbulence process itself and not set by the researchers. The very largest scales of the turbulence (which govern the decay behavior) are much larger than the initial mixing cube size. There is very little human input to the simulation that influences the

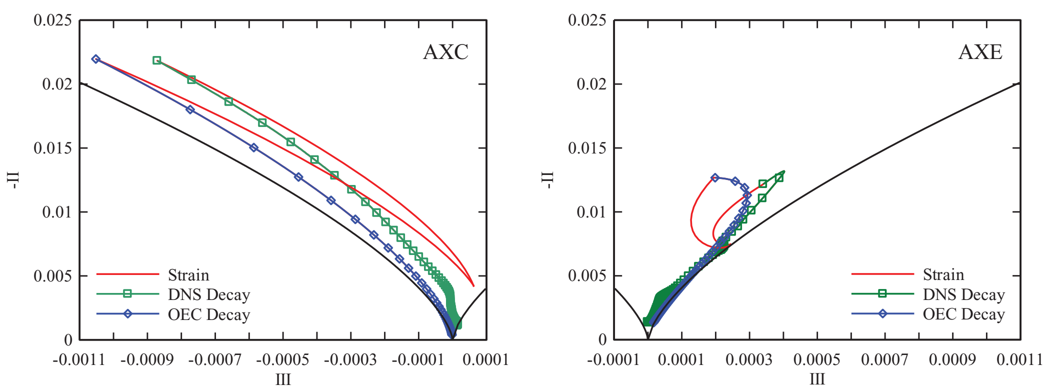

(a) (b)

FIG. 19. OEC vs. DNS: (a) AXC IC1and (b) AXE IC2 both subjected to high strain rate.

large scale turbulence. The very largest scales result from the Navier-Stokes equations and their interaction with a random arrangement of small cubes.

In these simulation at long times we do not see a return-to-isotropy, but a return to the background level of statistical anisotropy that the simulations began with. Comte-Bellot and Corrsin[41] make a similar observations in their experiments, as do Kang *et al.*[54] George[55] provides a possible theoretical argument for this behavior.

Because the large scales are much smaller than the domain size in these simulations, the turbulent Reynolds numbers are not large. Still, they are comparable to some experimental Reynolds numbers, and they appear to be high enough (at least for IC2) to produce the isotropic decay rate (n = 6/5) predicted by Saffman[46] for high Re turbulent decay both before and well after the straining process. It was found that the straining process, in both AXC and AXE, reduces the decay exponent (i.e., decay rate) in the highest strain rate cases and at least limits the increase of the decay rate in low strain rate cases. It was found that after straining, the decay rate increases to levels in the range of 6/5–3/2 Saffman's[46] predictions of high and low Reynolds number values. For cases of low strain rate both AXC and AXE can be seen to be increasing above the 3/2 level perhaps indicating a domain constrained condition (n = 2.0) (see Stalp *et al.*[47] and Touil *et al.*[56]).

An important observation of this paper is the confirmation that return-to-isotropy occurs in two stages, a ***recovery*** stage immediately after the strain is removed, in which some of the anisotropy components can still be increasing (and the decay rate differs from its isotropic value), and the ***return*** stage where the velocity fluctuation anisotropy tends to zero (and the classic isotropic decay rates are applicable). We hypothesize that the recovery stage is the turbulence structure (two-point correlation lengths) returning to isotropy at a faster rate than the velocity fluctuations return (which is the classic return stage). The observation in the DNS data of trajectory crossing supports the idea that the evolution of anisotropic turbulence cannot be captured by the information in the anisotropy tensor alone.

Traditional return-to-isotropy models are handicapped because they do not account for the presence of the recovery stage of anisotropic turbulent decay. It has been shown that even for the same mean flow conditions (i.e., AXC or AXE), different initial conditions produced quite different values of constants in the classic nonlinear return-to-isotropy models. Like the OEC model, the models of Kassinos and co-workers[53,52] can also predict the two stages of anisotropic decay, recovery, and return. The underlying models are related but not the same because of the difference in philosophy about what extra information is being included in the model (one-point correlations of derivatives versus two-point length scales). Both the modeling results of Kassinos and the current DNS work indicate that the recovery stage of anisotropic decay requires knowledge and representation of the turbulent structure.

This work only examines two types of anisotropic turbulence (AXC and AXE), but it is encouraging that the OEC model gives fairly reasonably predictions for all the different initial conditions and strain rates with a single set of constants.

ACKNOWLEDGMENTS

This work was supported by the National Science Foundation (CBET Grant No. 1032364). The bulk of these calculations were performed using NSF XSEDE supercomputing resources. These included, Ranger, provided by the Texas Advanced Computing Center at the University of Texas at Austin and Keeneland provided by NICS at the University of Tennessee.

[1] J. B. Perot, "Determination of the decay exponent in mechanically stirred isotropic turbulence," AIP Adv. **1**, 022104 (2011).
[2] C. J. Zusi and J. B. Perot, "Simulation and modeling of turbulence subjected to a period of uniform plane strain," Phys. Fluids **25**, 110819 (2013).
[3] G. I. Taylor, "Turbulence in a contracting stream," Z. Angew. Math. Mech. **15**, 91–96 (1935).
[4] A. A. Townsend, "The uniform distortion of homogeneous turbulence," Q. J. Mech. Appl. Math. **7**, 104 (1954).
[5] H. J. Tucker and A. J. Reynolds, "The distortion of turbulence by irrotational strain," J. Fluid Mech. **32**, 657–673 (1968).
[6] G. K. Batchelor and I. Proudman, "The efect of rapid distortion of a fluid in turbulent motion," Q. J. Mech. Appl. Math. **7**(1), 83 (1954).
[7] S. Chandrasekhar, "The theory of axisymmetric turbulence," Philos. Trans. R. Soc., A. **242**, 557–577 (1950).

[8] W. H. Matthaeus and C. Smith, "Structure of correlation tensors in homogeneous anisotropic turbulence," Phys. Rev. A **24**, 2135 (1981).
[9] C. Cambon and J. F. Scott, "Linear and nonlinear models of anisotropic turbulence," Annu. Rev. Fluid Mech. **31**, 1–53 (1999).
[10] M. Ould-Rouiss, "Axisymmetric form of Karman-Howarth equation and its limiting forms," Eur. Phys. J. B **15**, 339–347 (2000).
[11] M. S. Uberoi, "Effect of wind-tunnel contraction on free-stream turbulence," J. Aeronaut. Sci. **23**, 754–764 (1956).
[12] M. S. Uberoi, "Equipartition of energy and local isotropy in turbulent flow," J. Appl. Phys. **28**, 1165 (1957).
[13] G. Comte-Bellot and S. Corrsin, "The use of a contraction to improve the isotropy of grid-generated turbulence," J. Fluid Mech. **25**, 657 (1966).
[14] L. Le Penven, J. N. Gence, and G. Comte-Bellot, "On the approach to isotropy of homogeneous turbulence: Effect of the partition of kinetic nergy among the velocity components," in *Frontiers in Fluid Mechanics* (Springer, New York, NY, 1985), pp. 1–21.
[15] J. C. Rotta, "Statistische theorie nichthomogener turbulenz," Z. Phys. **129**, 547 (1951).
[16] J. L. Lumley and G. R. Newman, "The return to isotropy of homogeneous turbulence," J. Fluid Mech. **82**, 161–178 (1977).
[17] K.-S. Choi and J. L. Lumley, "Return to isotropy of homogeneous turbulence revisited," in *Turbulence and Chaotic Phenomena in Fluids*, edited by T. Tatsumi (North-Holland, 1983), pp. 267–272.
[18] T. Sjogren and A. V. Johansson, "Measurement and modeling of homogeneous asisymmetric turbulence," J. Fluid Mech. **374**, 59–90 (1998).
[19] O. Ertunc and F. Durst, "On the high contraction ration anomaly of axisymmetric contraction of grid-generated turbulence," Phys. Fluids **20**, 025103 (2008).
[20] S. Banerjee, O. Ertunc, C. Koksoy, and F. Durst, "Pressure strain rate modeling of homogeneous axisymmetric turbulence," J. Turbul. **10**(29), 1–39 (2009).
[21] U. Schumann and G. S. Patterson, "Numerical study of the return of axisymmetric turbulence to isotropy," J. Fluid Mech. **88**(4), 711–735 (1978).
[22] M. J. Lee and W. C. Reynolds, "Numerical experiments on the structure of homogeneous turbulence," Dissertation, Report TF-24 (Department of Mechanical Engineering, Thermoscience Division, Stanford University, 1985).
[23] L. Biferale, G. Boffetta, A. Celani, A. Lanotte, F. Toschi, and M. Vergassola, "The decay of homogeneous anisotropic turbulence," Phys. Fluids **15**, 2105 (2003).
[24] J. R. Chasnov, "The decay of axisymmetric homogeneous turbulence," Phys. Fluids **7**(3), 600 (1995).
[25] J. R. Herring, "Approach of axisymmetric turbulence to isotropy," Phys. Fluids **17**(5), 859 (1974).
[26] N. Nakauchi and H. Oshima, "The return of strongly anisotropic turbulence to isotropy," Phys. Fluids **30**, 3653 (1987).
[27] V. V. Mons, M. Meldi and P. Sagaut, "Numerical investigation on the partial return to isotropy of freely decaying homogeneous axisymmetric turbulence," Phys. Fluids **26**, 025110 (2014).
[28] S. C. Kassinos, W. C. Reynolds, and M. M. Rogers, "One-point turbulence structure tensors," J. Fluid Mech. **428**, 213–248 (2001).
[29] M. B. Martell and J. B. Perot, "The oriented-eddy collision model," Flow Turbul. Combust. **89**(3), 335–359 (2012).
[30] P. G. Saffman, "The large-scale structure of homogeneous turbulence," J. Fluid Mech. **27**, 581 (1967).
[31] S. M. de Bruyn Kops and J. J. Riley, "Direct numerical simulation of laboratory experiments in isotropic turbulence," Phys. Fluids **10**, 2125 (1998).
[32] J. C. del Alamo and J. Jimenez, "Spectra of the very large anisotropic scales in turbulent channels," Phys. Fluids, **15**, L41 (2003).
[33] F. H. Harlow and J. E. Welch, "Numerical calculation of time-dependent viscous incompressible flow of fluid with free surface," Phys. Fluids **8**(12), 2182 (1965).
[34] J. B. Perot, "An analysis of the fractional step method," J. Comput. Phys. **108**, 51 (1993).
[35] W. Chang, F. Giraldo, and J. B. Perot, "Analysis of an exact fractional step method," J. Comput. Phys. **179**, 1–17 (2002).
[36] J. B. Perot and P. Moin, "Shear-free turbulent boundary layers, Part I: Physical insights into near wall turbulence," J. Fluid Mech. **295**, 199 (1995).
[37] H. Le, P. Moin, and J. Kim, "Direct numerical simulation of turbulent flow over a backward step," J. Fluid Mech. **330**, 349 (1997).
[38] M. Martell, J. B. Perot, and J. Rothstein, "Direct numerical simulation of turbulent flow over drag-reducing ultrahydrophobic surfaces," J. Fluid Mech. **620**, 31 (2009).
[39] J. B. Perot, "Conservation properties of unstructured staggered mesh schemes," J. Comput. Phys. **159**(1), 58 (2000).
[40] J. B. Perot and V. Subramanian, "Discrete calculus methods for diffusion," J. Comput. Phys. **224**(1), 59 (2007).
[41] G. Comte-Bellot and S. Corrsin, "Simple Eularian time correlations of full and narrow-band velocity signals in grid generated isotropic turbulence," J. Fluid Mech. **48**, 273 (1971).
[42] L. Le Penven, J. N. Gence, and G. Comte-Bellot, "On the approach to isotropy of homogeneous turbulence: Effect of the partition of kinetic energy among the velocity components," in *Frontiers in Fluid Mechanics* (Springer, New York, NY, 1985), pp. 1–21.
[43] J. N. Gence and J. Mathieu, "The return to isotropy of an homogeneous turbulence having been submitted to two successive plane strains," J. Fluid Mech. **101**, 555 (1980).
[44] J. L. Lumley, "Computational modeling of turbulent flows," Adv. Appl. Mech. **18**, 123–176 (1979).
[45] K. Choi and J. L. Lumley, "The return to isotropy of homogeneous turbulence," J. Fluid Mech. **436**, 59–84 (2001).
[46] P. G. Saffman, "Note on decay of homogeneous turbulence," Phys. Fluids **10**, 1349 (1967).
[47] S. R. Stalp, "Decay of grid turbulence in a finite channel," Phys. Rev. Lett. **82**, 4831–4834 (1999).
[48] S. Sarkar and C. G. Speziale, "A simple nonlinear model for the return to isotropy in turbulence," Phys. Fluids **A**(2), 84 (1990).

[49] P. A. Durbin and B. A. P. Reif, *Statistical Theory and Modeling for Turbulent Flows*, 2nd ed. (John Wiley & Sons, Ltd, United Kingdom, 2001).
[50] K. S. Choi and J. L. Lumley, "Turbulence and chaotic phenomena in fluids," in *Proceedings of the IUTAM Symposium, Kyoto, Japan*, edited by T. Tatsumi (North-Holland, Amsterdam, 1984), p. 267.
[51] S. B. Pope, *Turbulent Flows* (Cambridge University Press, New York, NY, 2000).
[52] S. C. Kassinos and E. Akylas, "Advances in particle representation modeling of homogeneous turbulence. From the linear PRM version to the interacting viscoelastic IPRM," in *ERCOFTAC Series 18, New Approaches in Modeling Multiphase Flows and Dispersion in Turbulence, Fractal Methods and Synthetic Turbulence*, edited by F. C. G. A. Nicolleau, C. Cambon, and J.-M. Redondo (Springer, New York, 2012), pp. 81–101.
[53] S. C. Kassinos, C. A. Langer, S. L. Haire, and W. C. Reynolds, "Structure-based turbulence modeling for wall-bounded flows," Int. J. Heat Fluid Flow **21**, 599–605 (2000).
[54] H. S. Kang, S. Chester, and C. Meneveau, "Decaying turbulence in an active-grid-generated flow and comparisons with large-eddy simulation," J. Fluid Mech. **480**, 129–160 (2003).
[55] W. K. George, "Is there an asymptotic effect of initial and upstream conditions on turbulence?," in Freeman Lecture, ASME Fluids Engineering Meeting, Jacksonville, FL, USA, 2008.
[56] H. Touil, J. P. Bertoglio, and L. Shao, "The decay of turbulence in a bounded domain," J. Turbul. **3**, 49 (2002).